Optical spectroscopy of a microsized Rb vapor sample in magnetic fields up to 58 T

D. Ciampini*
Dipartimento di Fisica "E. Fermi," Università di Pisa, Largo B. Pontecorvo 3, 56127 Pisa, Italy;
INO-CNR, Via G. Moruzzi 1, 56124 Pisa, Italy;
and CNISM, UdR Dipartimento di Fisica "E. Fermi," Università di Pisa, Largo B. Pontecorvo 3, 56127 Pisa, Italy

R. Battesti and C. Rizzo
Laboratoire National Des Champs Magnétiques Intenses (UPR 3228, CNRS-UPS-UGA-INSA), F-31400 Toulouse Cedex, France

E. Arimondo
Laboratoire National des Champs Magnétiques Intenses (UPR 3228, CNRS-UPS-UGA-INSA), F-31400 Toulouse Cedex, France;
Dipartimento di Fisica "E. Fermi," Università di Pisa, Largo B. Pontecorvo 3, 56127 Pisa, Italy;
and INO-CNR, Via G. Moruzzi 1, 56124 Pisa, Italy

(Received 1 August 2017; published 14 November 2017)

We use a magnetometer probe based on the Zeeman shift of the rubidium resonant optical transition to explore the atomic magnetic response for a wide range of field values. We record optical spectra for fields from a few tesla up to 60 T, the limit of the coil producing the magnetic field. The atomic absorption is detected by the fluorescence emissions from a very small region with a submillimeter size. We investigate a wide range of magnetic interactions from the hyperfine Paschen-Back regime to the fine one and the transitions between them. The magnetic field measurement is based on the rubidium absorption itself. The rubidium spectroscopic constants were previously measured with high precision, except the excited state Landé g-factor that we derive from the position of the absorption lines in the transition to the fine Paschen-Back regime. Our spectroscopic investigation, even if limited by the Doppler broadening of the absorption lines, measures the field with a 20 ppm uncertainty at the explored high magnetic fields. Its accuracy is limited to 75 ppm by the excited state Landé g-factor determination.

DOI: 10.1103/PhysRevA.96.052504

I. INTRODUCTION

The present large effort of the quantum control research is the miniaturization and manipulation from the micron scale down to the single atom. This objective is important for a complete quantum control and for the development of new tools for applications, such as geophysics, biophysics, brain imaging, and more. Recently much attention was concentrated on the magnetic response and the measurement of weak magnetic fields with a high spatial resolution. Technologies capable of micron-scale magnetic microscopy include superconducting quantum interference devices (SQUIDs), scanning Hall probe microscopes, magnetic force microscopes, and magneto-optical imaging techniques. Magnetic fields may also be measured by detecting the Zeeman splitting for warm and ultracold atoms [1,2], nuclei in a ferromagnetic material [3], or impurities in diamond (NV centers) [4–6].

The same amount of attention was not reserved to the measurement of high magnetic fields, whose application range is steadily growing. Nowadays accurate measurements of high magnetic fields are performed via the Zeeman splitting in nuclear magnetic resonance of hydrogen in water. This technique based on radiofrequency or microwave frequency absorption is applied mainly to continuous magnetic fields, with an uncertainty better than 1 ppm over a volume of a few mm^3. As is well known from optical pumping, the detection of higher energy photons, i.e., as optical ones, greatly increases the measurement efficiency [7]. In the presence of an applied magnetic field, atomic optical transitions experience a Zeeman frequency shift, and today laser frequencies are measured with very high precision. The measure of a Zeeman shift is routinely applied to the magnetic field in plasmas produced by an exploding wire [8–11], where the high sample temperature limits the precision.

We have developed an optical spectroscopy magnetic field probe based on the Zeeman splitting in a rubidium atomic sample with a volume of 0.11 mm^3 [12]. The present investigation of atomic spectroscopy at high magnetic fields is based on that probe. Our experiment operates with pulsed magnetic fields having rise and fall times around 100 ms. Even if the detection is based on Doppler limited absorption spectroscopy, at the explored fields around 60 T the reached 20 ppm uncertainty allows us to perform high-resolution optical spectroscopy.

We report a precise study of the Zeeman effect for the rubidium $5\,^2S_{1/2} \rightarrow 5\,^2P_{3/2}$ resonance line in magnetic field regimes not well explored. Our results demonstrate that under a high-resolution investigation the classification of the regimes as hyperfine or fine Paschen-Back ones [13] represents a rough schematization for the atomic response. The data evidence that the hyperfine Paschen-Back regime is fully reached at magnetic fields larger than the standard comparison between electronic Zeeman energy and hyperfine structure splitting. On the other hand, a theoretical description based on the fine Paschen-Back approach is required to interpret data collected at magnetic fields lower than the standard comparison between electronic Zeeman energy and fine structure splitting.

*donatella.ciampini@unipi.it

As original feature, our measurement does not rely on the presence of an independent magnetometer, and the magnetic field value is derived directly from the measured rubidium optical absorption. The determination is based on the existence of an optical Zeeman shift characterized by a field linear dependence at all magnetic field values. That measurement combined with the magnetic field temporal evolution detected by a pick-up coil provides the absolute scale for the whole explored magnetic range. All atomic constants determining the rubidium absorption frequencies are well known from previous investigations, except for the Landé g-factor of the excited $5P$ state. Within the target of using the rubidium optical transitions for an atomic magnetometer, its precise value is required. We have derived the excited state Landé g-factor by exploring the magnetic field dependence of different optical transitions. The ratio of the associated resonance fields, independent of the magnetic field absolute calibration, provides this atomic constant with high precision. The accuracy of the rubidium-based magnetometry is limited to 75 ppm by our g-factor uncertainty.

Section II describes the response to high magnetic fields, presenting eigenstates, eigenenergies, and optical transitions starting from the hyperfine Paschen-Back approximation. The diamagnetic contribution to the rubidium energy levels of interest is discussed. We introduce the optical transition line used for the magnetic field calibration. The section is completed by a brief discussion of the atomic magnetic data required for our analyses. Section III describes the experimental setup, with the absorption detection based on the fluorescence detection in order to decrease the observation volume. Section IV reports examples of recorded spectra, their analysis, and the role played by the nuclear interaction. This section includes also an analysis of the ratio of the high and low magnetic resonant fields for the σ^+ lines. The modification of the full fine structure multiplet is required for the data interpretation leading us to the Landé g-factor determination. A final section concludes our work.

II. RUBIDIUM IN A HIGH MAGNETIC FIELD

A. Paramagnetism

For an alkali atom, the magnetic interaction of the valence electron is described through several quantum numbers, for the nucleus the (I,m_I) spin components, and for the electron the (L,m_L) orbital angular momentum, the (S,m_S) spin, the vector composition of $\mathbf{L}$ and $\mathbf{S}$ with (J,m_J) components, and finally the vector composition of $\mathbf{J}$ and $\mathbf{I}$ with components (F,m_F). As in textbooks [13], at very low magnetic fields, where the electron-nucleus hyperfine interaction is larger than the electronic Zeeman interaction, (F,m_F) are the correct quantum numbers. Increasing the magnetic field the hyperfine Paschen-Back regime is reached when the role between hyperfine interaction and electronic Zeeman energy is reversed [13]. There (J,m_J) are the good quantum numbers. Because for rubidium the $5\,^2S_{1/2}$ ground state hyperfine interaction is around 50 times larger than the $5\,^2P_{3/2}$ excited state one, the hyperfine Paschen-Back regime should be reached when the electron Zeeman energy is roughly equal to the ground state interaction, around 0.5 T for ^{87}Rb. While for the ground state (J,m_J) remain good quantum numbers for all higher magnetic fields, for the excited state the fine structure splitting between $5\,^2P_{1/2}$ and $5\,^2P_{3/2}$ states must be compared to the electronic Zeeman splitting. For rubidium the fine Paschen-Back regime is reached at fields around 500 T. There $(L=1,m_L)$ and $(S=1/2,m_S)$ are the quantum numbers, combined with the nuclear spin. This regime was never explored in rubidium, while owing to the smaller fine structure splitting it was explored for sodium in experiments with exploding wires [8–11].

At high fields the diamagnetism contribution to the magnetic interaction should be included in the analysis, as in Sec. II C. However, our experiment demonstrates this contribution negligible for fields up to 60 T. For completeness Refs. [14,15] explored for the rubidium ground state a Zeeman energy term induced by the magnetic dipole hyperfine interaction, through a coupling of higher electronic levels into the ground state, a term quadratic in m_I and equivalent to a modification of the nuclear g-factor. This shift is only a few Hz at our largest explored field.

Following the above classification, the 1–60 T explored magnetic field range corresponds to the hyperfine Paschen-Back regime. Thus the rubidium ground state is specified by $(J_g=1/2,m_{Jg})$, combined with (I,m_I). The two stable isotopes, ^{85}Rb and ^{87}Rb, have nuclear spin, $I=5/2$ and $I=3/2$, respectively, characterized by the nuclear Landé g-factor g_I, assumed negative as in Ref. [16]. For the alkali ground state, the eigenenergies are given by the Breit-Rabi formula [13,17], including the electronic and nuclear Zeeman energies and the A_g dipolar hyperfine coupling.

For the excited state, no analytical formula exist for the eigenenergies, to be derived by diagonalizing numerically the Hamiltonian. For the hyperfine Paschen-Back regime the Hamiltonian contains the magnetic interactions and the hyperfine dipolar (A_e) and quadrupolar (B_e) contributions. For the fine Paschen-Back regime, the Hamiltonian includes the above contributions and the fine structure splitting of the excited $5\,^2P_{1/2,3/2}$ states.

For an applied B field and in the hyperfine Paschen-Back regime, the energies of the ground and excited states, E_g and E_e, respectively, expressed in frequency units are given by

$$E_g(J_g=1/2,m_{Jg};I,m_{Ig})=\mu_B(g_{5S}m_{Jg}+g_Im_{Ig})B+A_gm_{Jg}m_{Ig},$$

$$E_e(J_e=3/2,m_{Je};I,m_{Ie})=\mu_B(g_{5P_{3/2}}m_{Je}+g_Im_{Ie})B+A_em_{Je}m_{Ie}+B_e\frac{6(m_{Je}m_{Ie})^2+3m_{Je}m_{Ie}-2I(I+1)J_e(J_e+1)}{4I(2I-1)J_e(2J_e-1)}, \quad (1)$$

where μ_B is the Bohr magneton in MHz/T, and g_{5S} and $g_{5P_{3/2}}$ are the electronic Landé g-factors. For the investigated magnetic field range the nuclear Zeeman contribution is larger than the hyperfine coupling for the excited state, and comparable for the ground state. That determines different dependences of the state energy on the nuclear quantum number, as shown in Figs. 1(a) and 1(b).

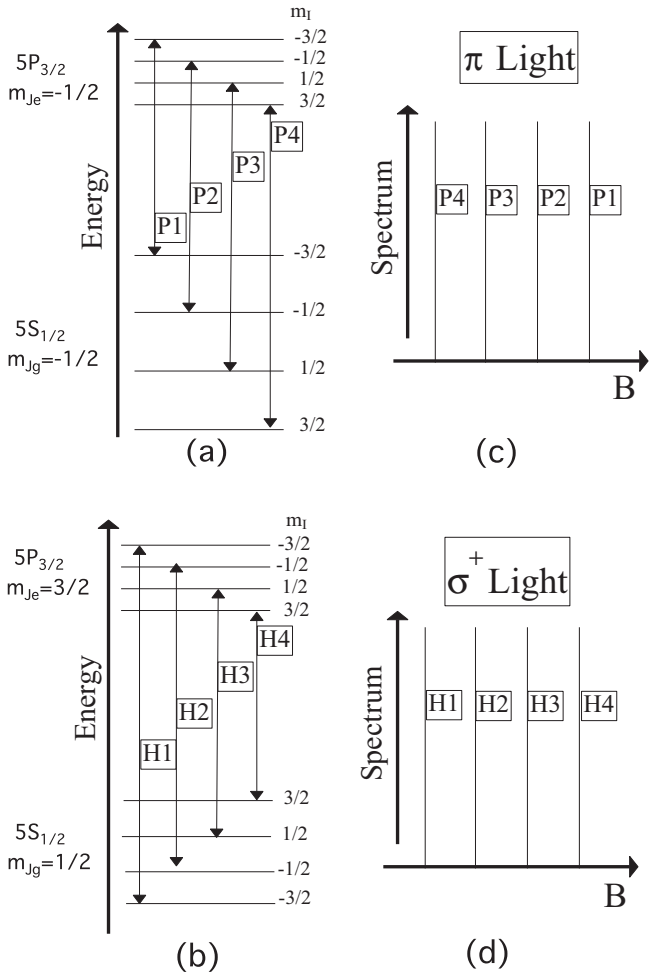

FIG. 1. (a) and (b) Energy levels at a given B value. (c) and (d) The spectrum produced by transitions between the levels of (a) and (b), respectively, at a given laser frequency and scanning the B magnetic field. The top and bottom plots correspond to the nuclear components of different electronic ground or excited states. Panels (a) and (c) correspond to the $|J_g = 1/2, m_{Jg} = -1/2\rangle \rightarrow |J_e = 3/2, m_{Je} = -1/2\rangle$ π transitions, denoted as πPi with $(i = 1,4)$. Panels (b) and (d) correspond to the $|J_g = 1/2, m_{Jg} = 1/2\rangle \rightarrow |J_e = 3/2, m_{Je} = 3/2\rangle$ σ^+ transitions, denoted as σ^+Hi. Notice the energy order of the nuclear levels for different electronic states, producing a different order of the πPi and σ^+Hi lines while scanning B.

B. Absorption lines

The energy levels and the optical transitions are discussed here for the ^{87}Rb isotope with $I = 3/2$. For a given magnetic field B and a given laser frequency ν_L, the absorption spectrum is composed by lines at frequencies

$$\nu_L = \nu_0 + \left[E_e\left(\tfrac{3}{2}, m_{Je}; \tfrac{3}{2}, m_{Ie}\right) - E_g\left(\tfrac{1}{2}, m_{Jg}; \tfrac{3}{2}, m_{Ig}\right)\right], \quad (2)$$

where ν_0 is the rubidium absorption center of gravity at $B = 0$. Within the strong magnetic field regimes the light induces mainly transitions with $\Delta m_I = 0$ selection rules. Because of the small diamagnetic contributions, as in Secs. II C and IV A, the position of absorption lines is dominated by the paramagnetic contributions of Eqs. (1).

Our experimental approach is based on imposing an offset $\Delta\nu_L = \nu_L - \nu_0$ and pulsing the magnetic field from zero to a preset maximum value. At specific times the atoms reach a resonance with the laser by the Zeeman effect. The fluorescence emission monitors the atomic absorption. For our $\Delta\nu_L$ positive values, the spectra observed by scanning the magnetic field contain three sets of lines, denoted πPi, σ^+Hi, and σ^+Li, starting from a high resonant field to a low one, with $(i = 1,4)$ corresponding to the $(m_I = \pm 3/2, \pm 1/2)$ components.

The π polarized Pi lines, produced by the $|J_g = 1/2, m_{Jg} = -1/2\rangle \rightarrow |J_e = 3/2, m_{Je} = -1/2\rangle$ transitions, experience the smallest Zeeman shift. Figure 1(a) shows the energy levels corresponding to these transitions at given B. Figure 1(c) schematizes their nuclear structure as observed at fixed $\Delta\nu_L$ and scanning B.

Figure 1(b) shows the energy levels corresponding to the $|J_g = 1/2, m_{Jg} = 1/2\rangle \rightarrow |J_e = 3/2, m_{Je} = 3/2\rangle$ σ^+Hi polarized transitions at fixed B. The ground state nuclear structure is dominated by the hyperfine interaction even at the highest explored magnetic field and produces an opposite ranking of the m_I levels in Figs. 1(a) and 1(b) because of the different m_{Jg} sign. The excited state nuclear structure, dominated by the nuclear Zeeman effect, is the same for the two cases. As a consequence scanning the B field, the order of the lines is opposite for the πPi and σ^+Hi cases, as in Figs. 1(c) and 1(d). The centers of gravity of the absorption lines eliminating the hyperfine structure contribution play a key role in our data analysis. For both hyperfine and fine Paschen-Back regimes the center of gravity for the σ^+Hi transitions is

$$B^H_{\text{Center}} = \frac{\Delta\nu_L}{\mu_B(3g_{5P_{3/2}} - g_{5S})/2}. \quad (3)$$

Similar σ^+ transitions denoted σ^+Li are the $|J_g = 1/2, m_{Jg} = -1/2\rangle \rightarrow |J_e = 3/2, m_{Je} = 1/2\rangle$ ones. These transitions appear at a magnetic field lower than the previous ones, because they experience a larger Zeeman shift. The order of the σ^+Li lines observed while scanning the magnetic field is reversed in respect to that of the σ^+Hi lines and similar to the πPi ones. For the hyperfine Paschen-Back regime only, the center of gravity of the σ^+Li transitions is

$$B^L_{\text{Center}} = \frac{\Delta\nu_L}{\mu_B(g_{5P_{3/2}} + g_{5S})/2}. \quad (4)$$

Within the hyperfine and fine Paschen-Back regimes, the πPi, σ^+Hi, and σ^+Li nuclear transitions are not equally spaced, because of the small excited state hyperfine quadrupole coupling.

C. Diamagnetism

Diamagnetic corrections are necessary for accurate measurements at high magnetic fields. If the magnetic perturbation is smaller than the energy separation between states with different L quantum numbers, the E^{dia} diamagnetic energy for a single valence electron may be written

$$E^{\text{dia}} = \xi^{\text{dia}} B^2 \quad (5)$$

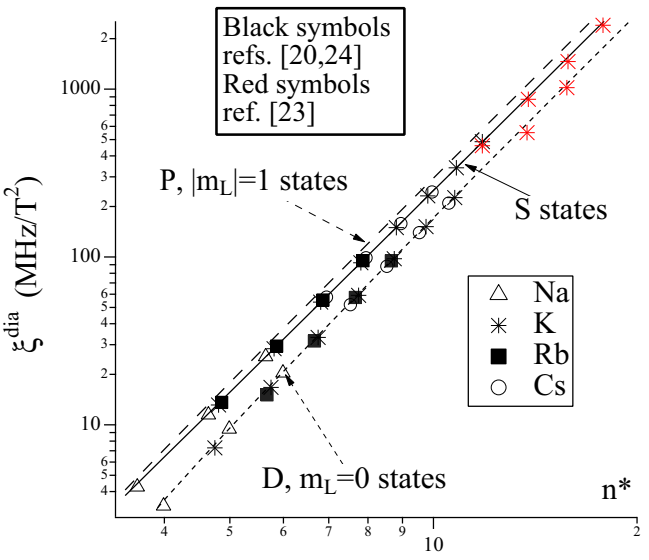

FIG. 2. Experimental results and theoretical predictions of $\xi^{\rm dia}$ vs the n^* effective quantum number for S, $(P,m_L=\pm1)$ and $(D,m_L=0)$ low-energy states of alkalis. Equation (6) predictions for those states correspond to the continuous, dashed, and dotted lines, respectively. Triangles, stars, filled squares, and open circles refer to Na, K, Rb, and Cs results, respectively, measured in the references reported within the top box. For our $5S$ and $5P$ states the n^* values are 1.81 and 2.30, respectively.

on the basis of the susceptibility $\xi^{\rm dia}$. Within an hydrogen-like description, for an electron with quantum numbers n,L,m_L, and an effective quantum number $n^*=n-\delta$ determined by the quantum defect δ, $\xi^{\rm dia}$ derived by Refs. [18,19] was rewritten by Ref. [20] as

$$\xi^{\rm dia}=\frac{5e^2a_0^2}{8\mu_e}\left[1+\frac{1-3l(l+1)}{5(n^*)^2}\right]\frac{l(l+1)+m_l^2-1}{(2l-1)(2l+3)}(n^*)^4, \tag{6}$$

with a_0 the Bohr radius, e the electron charge, and μ_e the electron reduced mass.

Figure 2 reports experimental determinations and theoretical predictions for $\xi^{\rm dia}$ versus n^* in alkalis for low n quantum numbers. Early measurements were performed on P states in Na and K at 2.7 T [21] and in K, Rb, Cs at 2.3 T [22]. The diamagnetic contribution was measured using two-photon spectroscopy excited S and D states originally by Ref. [23], and later more systematically for all alkalis by Refs. [20,24]. The measurements by Ref. [20] for S and D states on different alkalis span n quantum numbers as low as three. The simple hydrogen atom description of Eq. (6) with quantum defects derived from Refs. [25,26] provides a good fit to the susceptibilities of the figure. The P states measurements by Refs. [21,22] on several alkalis focused on quantum numbers between 12 and 30. Those low-precision data are also fitted by that equation, except that for Rydberg states with $n>20$ the inter-L perturbation interactions introduce deviations from the predicted values.

Equation (6) predicts the $\xi^{\rm dia}$ diamagnetic values of $0.29\,{\rm MHz/T^2}$ and $0.68\,{\rm MHz/T^2}$, respectively, for our $5S$ and $5P$ states. That leads to a predicted $\Delta\nu^{\rm dia}=0.39\,{\rm MHz/T^2}$ diamagnetic shift for the σ^+H4 line, compared to its $\approx$14 GHz/T paramagnetic shift. All these values should be considered only as an order of magnitude, because of the limited validity of the hydrogen-like description for our states with the low n^* values reported in the figure caption. At 58 T the predicted diamagnetic shift is around 1.3 GHz, corresponding to about three times the Doppler line width of the absorption lines, whence measurable. Our $\xi^{\rm dia}$ result is presented at the end of Sec. IV A.

D. Data analysis

Our ^{87}Rb spectral analysis is based on the atomic constants reported in Ref. [27], except for the Landé g-factors. For ^{87}Rb the ground state Landé g-factor was precisely measured in Ref. [28] with respect to the g_e free electron g-factor. Making use of the g_e value given in Ref. [29] we obtain $g_{5S}=2.002331070(26)$. A larger indetermination is associated to the Landé $g_{5P_{3/2}}$-factor. The data of Ref. [16] point out that for all the alkali atoms the g-factor of the first excited $P_{3/2}$ state is $\approx$1.33411, as predicted by the Russel-Saunders coupling between the orbital magnetic moment, with $g_L=1$, and the spin magnetic moment, using g_e or g_{5S}. For the ^{87}Rb $5P_{3/2}$ state, Ref. [16] reported 1.3362(13) as a weighted average of all the measurements available at that time and still today. That value is largely determined by fitting the level crossing measurements by Belin and Svanberg [30], who derived simultaneously $g_{5P_{3/2}}$ and the dipolar and quadrupolar hyperfine constants. We have reanalyzed those level-crossing measurements by fixing the hyperfine constants to the very precise values of Ref. [31] reported in Ref. [27] and using the ^{87}Rb nuclear magnetic moment of Ref. [16]. A new $g_{5P_{3/2}}=1.3341(2)$ value is obtained, in agreement with the above Russel-Saunders prediction, to be used as the starting point of our analysis. Following Ref. [32–35], QED and relativistic corrections are at the level of 10^{-4}–10^{-5}.

E. Rb atom as magnetometer

Our magnetic field determination is based on the rubidium spectrum itself. It relies on the existence of two eigenstates, ground and excited, denoted as extreme, whose energy dependence on the magnetic field is exactly linear, excluding the diamagnetic contribution. These eigenstates correspond to the highest values of all the atomic quantum numbers. The $5\,^2S_{1/2}\,|J_g=1/2,m_{gJ}=1/2;I,m_{gI}=I\rangle$ ground state has the following energy:

$$E_g^+=\mu_B\left(\frac{g_{5S}}{2}+g_I I\right)B+\frac{1}{2}A_g I. \tag{7}$$

The excited eigenstate with the highest energy, i.e., the $5P_{3/2}\,|J_e=3/2,m_{eJ}=3/2;I,m_{eI}=I\rangle$ state, has the following energy whichever magnetic field value:

$$E_e^+=\mu_B\left(\frac{3g_{5P_{3/2}}}{2}+g_I I\right)B+\frac{3}{2}A_e I+\frac{1}{4}B_e. \tag{8}$$

These formulas for the extreme states, even if derived from Eqs. (1) valid in the hyperfine Paschen-Back regime, apply to all regimes, even for the fine Paschen-Back one.

Combining Eqs. (2), (7), and (8), the Zeeman frequency shift of the σ^+H4 optical transition linking the Rb linear

dependent states is given by

$$\Delta\nu_L(\sigma^+H4) = \mu_B B\frac{3g_{5P_{3/2}} - g_{5S}}{2} + \frac{I}{2}(3A_e - A_g) + \frac{1}{4}B_e. \tag{9}$$

The inversion of this equation allows us to derive the B value from the laser frequency exciting the Rb atoms.

For our Doppler limited spectroscopy with the Gaussian absorption center determined at one twentieth of its line width, the magnetic field precision is ≈0.002 T. The above determination leads to the 20 ppm precision at high fields. The Rb magnetometry accuracy is determined by the $g_{5P3/2}$ uncertainty, 750 ppm for the value reported in Ref. [16], and 75 ppm for the value derived in Sec. IV.

III. PROBE AND MAGNET

The experimental setup is based on a rubidium probe located in the room temperature bore of a liquid nitrogen-cooled magnet, as detailed in Ref. [12]. The probe is composed by a quartz cell located at the end of a long pipe placing the cell within the magnet and hosting all the electrical and optical connections. The cell with $3 \times 3 \times 30$ mm^3 internal dimensions is filled with natural rubidium. As in the top of Fig. 3, a single-mode optical fiber provides the input beam, while the transmitted light and the atomic fluorescence emission reach the outside detectors through multimode fibers. Before entering into the cell the light, generated by a DLX100 Toptica laser, is polarized at 45° with respect to the magnetic field direction in order to induce both π and σ transitions. The Faraday rotation, experienced by the light propagating through the input single mode fiber and parallel to the magnetic field direction, modifies the total intensity, not the polarization on the atoms. The reported data for a laser intensity 15 times the saturation intensity are produced by a few ten thousand atoms. Previous tests, performed before assembling the cell within the magnet, demonstrated that the minimum number of detectable atoms is around 100. The fluorescence observation instead of the transmission allows us to reduce the influence of the magnetic field inhomogeneity. In fact from the fiber diameter and the collection lens parameters, we evaluate that the fluorescence light is produced from a $0.4 \times 0.4 \times 0.7$ mm^3 volume, smaller than the cell volume probed by transmission.

The 60 T pulsed magnetic field coil, a standard one at the High-Field National Laboratory (LNCMI) in Toulouse, has a 28 mm free bore diameter and is immersed into the liquid nitrogen in order to facilitate the heat dissipation [36]. The magnetic field homogeneity on the probed atomic volume is estimated better than 10 ppm. The rise time and decay time of the field temporal evolutions are around 55 and 100 ms, respectively, as shown in the bottom of Fig. 3. The field temporal evolution is monitored by a pick-up coil located at 7 mm from the atoms. Its frequency response bandwidth is larger than 500 kHz. The pick-up signal is calibrated in a separate carefully designed solenoid. The integrated pick-up signal reproduces the time profile of the magnetic pulse. That signal, corrected for the distance from the probe center position, provides a reference measurement B_{PU} of the magnetic field experienced by the atoms. The field calibration is based on the B_{H4} theoretical prediction for the σ^+H4

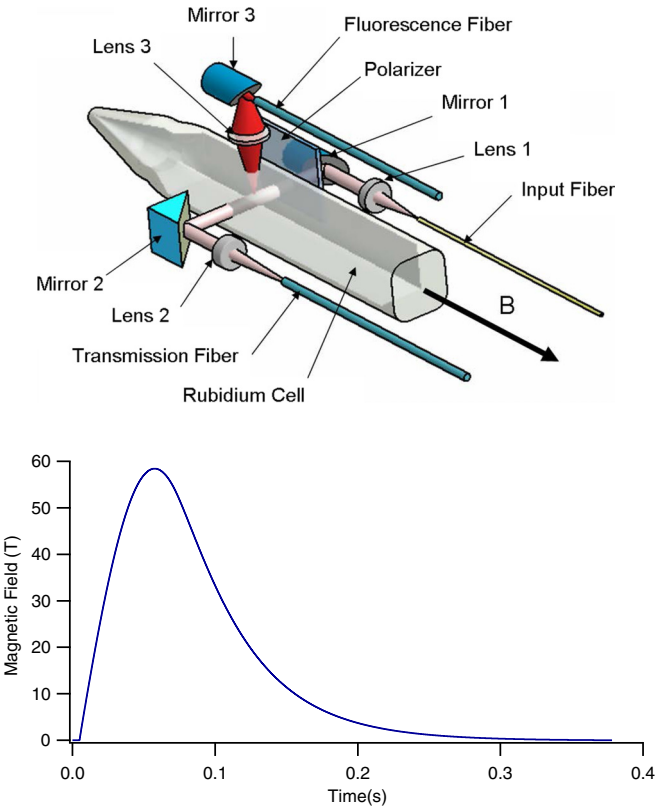

FIG. 3. On the top, optical scheme of the Rb cell with a single mode fiber for the laser input and multimode fibers for the transmission light and the fluorescence light output. Matching lenses and a 45° linear polarizer controlling the light reaching the Rb atoms are shown. The cell is oriented parallel to the B field direction, and the interrogation light propagates orthogonally to the field. On the bottom, magnetic field temporal dependence for a typical pulse.

resonance derived from Eq. (9) at a given laser frequency. From the analysis of ≈70 spectra, a linear dependence between B_{PU} and B_{H4} was verified, with slope 0.9899(2) using the Russell-Saunders g-factor reported above.

While the coil current is pulsed on-off, the atomic fluorescence and/or absorption signal is recorded as a function of time. The time-dependent magnetic field pick-up signal is recorded simultaneously. The combination of these two signals produces the magnetic field dependence of the atomic signal presented in the spectra of the following section.

IV. EXPERIMENTAL RESULTS

A. Spectra

Figure 4 reports examples of the fluorescence spectra versus the magnetic field for two different values of the $\Delta\nu_L$, both of them reconstructed from signals recorded during the rise of the current pulse. Similar spectra are obtained during the fall of the coil current. The top spectrum, obtained for a low $\Delta\nu_L$, is characterized by the presence of all the σ^+Li, σ^+Hi and πPi lines in sequence at increasing B values. The lines at higher B values experience a smaller Zeeman shift. The intensities are proportional to the theoretically predicted line strengths. In the bottom spectrum, obtained for a large

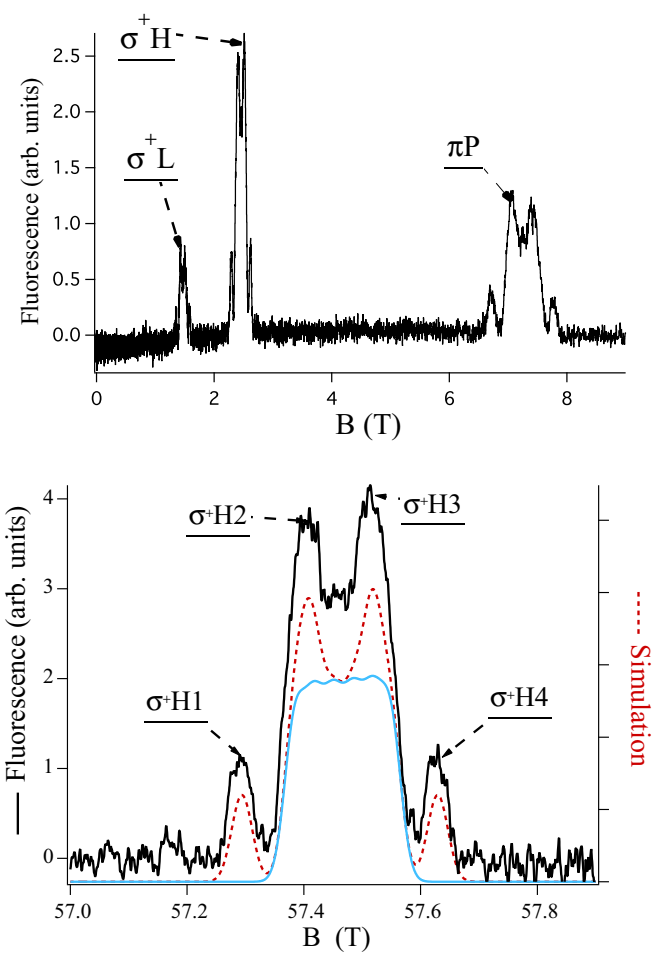

FIG. 4. Rb fluorescence spectra observed by scanning the magnetic field, on the top for $\Delta\nu_L = 34.692(5)$ and on the bottom for $\Delta\nu_L = 812.331(5)$, all in GHz, with uncertainty given by the accuracy of the wavelength meter reading. For both spectra the sinusoidal periodic fluorescence variation produced by the fiber Faraday effect was subtracted. The bottom plot, on an expanded scale, shows the individual σ^+Hi lines for a very high magnetic field. The quantum number assignment is in Fig. 1. Each fluorescent structure is composed of four resolved lines associated to the ^{87}Rb nuclear spin states and by a central unresolved broad structure associated to the ^{85}Rb nuclear components. The dotted red line reports a simulation including the Gaussian Doppler broadening for each absorption line, while the blue continuous line reports only the ^{85}Rb contribution, with an offset for both of them, for presentation clarity. The simulation only free parameter is the overall scale.

$\Delta\nu_L$, the σ^+Hi lines appear for a magnetic field close to the coil maximum operational current. The horizontal scales are obtained combining the information provided by the B_{H4} value and the temporal magnetic field dependence measured by the pick-up coil.

Each fluorescent set includes the ^{85}Rb and ^{87}Rb contributions. The four-peak structure observed for each set corresponds to the nuclear structure of the ^{87}Rb $I = 3/2$ spin. Because for ^{85}Rb the A_g hyperfine coupling is two times smaller than for ^{87}Rb, and because of its higher spin value $I = 5/2$, the nuclear structure cannot be resolved by the Doppler limited spectroscopy. We have performed simulations of the spectra including the Doppler Gaussian broadening, an example represented by the red dotted line of the bottom panel of Fig. 4. The simulation reproduces the four ^{87}Rb σ^+Hi lines having the same intensity and the central broadening due to the unresolved ^{85}Rb lines. On the bottom spectrum, the asymmetry between the two sides of the absorption structure, clearly visible on the ^{85}Rb simulation, is produced by the unequal spacing among the nuclear levels, around 0.002 T in the resonant magnetic field.

Analyzing spectra obtained for different $\Delta\nu_L$ values, we derive the linear relation between B_{PU} and B_{H4} reported within Sec. III. In order to test the presence of a quadratic diamagnetic nonlinearity, we repeat the previous analysis of B_{PU} versus B_{H4} by including into the fit function a quadratic term. The fit quality is not improved, and the derived $\xi^{\rm dia}$ value is smaller than the above theoretical prediction by a factor of 10 and compatible with zero owing to a large error bar.

B. Ratio between $B^H_{\rm Center}$ and $B^L_{\rm Center}$

This subsection targets the $g_{5P_{3/2}}$ value that among the Rb data has a low accuracy. Equations (3) and (4) show the different dependence of $B^H_{\rm Center}$ and $B^L_{\rm Center}$ on $g_{5P_{3/2}}$ because of the different excited state m_{Je} quantum numbers. Those equations don't have the same regime of validity: the $B^H_{\rm Center}$ expression is valid at all fields; the $B^L_{\rm Center}$ is based on the hyperfine Paschen-Back approximation. Within this approximation, at high magnetic fields, for a given $\Delta\nu_L$ laser detuning the $B^H_{\rm Center}/B^L_{\rm Center}$ ratio is a constant. This prediction is shown by the dotted blue line in Fig. 5, where also the experimental results for the ratio are plotted as function of $\Delta\nu_L$ on the bottom axis, or the corresponding $B^H_{\rm Center}$ center on the top axis. Notice the high precision reached by the measurements at very high fields, where the Doppler line width is a small fraction of the Zeeman shift. Our data do not follow the constant value theoretically predicted by the dotted line of the hyperfine Paschen-Back description. Instead the ratio increases with the $\Delta\nu_L, B^H_{\rm Center}$ values.

After excluding technical issues, as the shift of the probe position within the magnet at very high fields, we have searched a different explanation. As in Sec. II A, for the rubidium first resonance line the fine Paschen-Back regime is fully reached for a magnetic field around 500 T. Figure 5 explores a range of B values lower than this limit. Nevertheless we have calculated the eigenergies of all the fine structure levels, i.e.,, both $5\,^2P_{3/2}$ and $5\,^2P_{1/2}$ states, including the hyperfine outdiagonal matrix elements as in Ref. [16]. The operating magnetic field, "low" for fully reaching the fine Paschen-Back regime, produces a deviation of the $|5\,^2P_{3/2}; J_e = 3/2, m_{Je} = 1/2; I, m_{Ie}\rangle$ energies (those of the σ^+Li transitions) from the hyperfine Paschen-Back prediction, at the $\approx 10^{-4}$ level. As a consequence also the $B^H_{\rm Center}/B^L_{\rm Center}$ ratio is modified.

As starting point, the theoretical analysis for the fine Paschen-Back regime is based on the orbital Landé g_L-factor equal 1 and the spin g_S-factor equal to g_{5S}, leading within the Russell-Saunders coupling to the $g_{5P_{3/2}}$ value presented in Sec. II D. This analysis, represented in Fig. 5 by the black dashed line, reproducing the observed behavior at

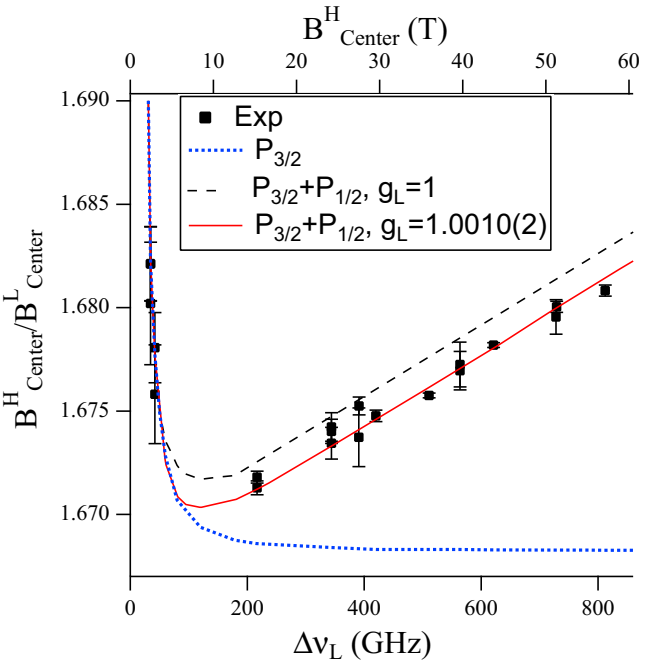

FIG. 5. Ratio between BH_{Center} and BL_{Center} magnetic fields vs the $\Delta\nu_L$ laser detuning (bottom axis) and BH_{Center} value (top axis). Squares for the measured values, including error bars, in several cases smaller than the square. Lines report theoretical predictions. The dotted blue line is based on the $5\,^2P_{3/2}$ eigenergies, at high magnetic fields leading to the hyperfine Paschen-Back regime with a constant value of the ratio. The black dashed line and the red continuous line are based on the magnetic eigenenergies of the whole fine structure $5\,^2P_{3/2}$ and $5\,^2P_{1/2}$ manifold, describing at high fields the fine Pachen-Back regime. Different g_L values, shown in the inset, with $g_S = g_{5S}$, are used for the two cases. The red line results are obtained for other [g_L, g_S] combinations discussed in the text.

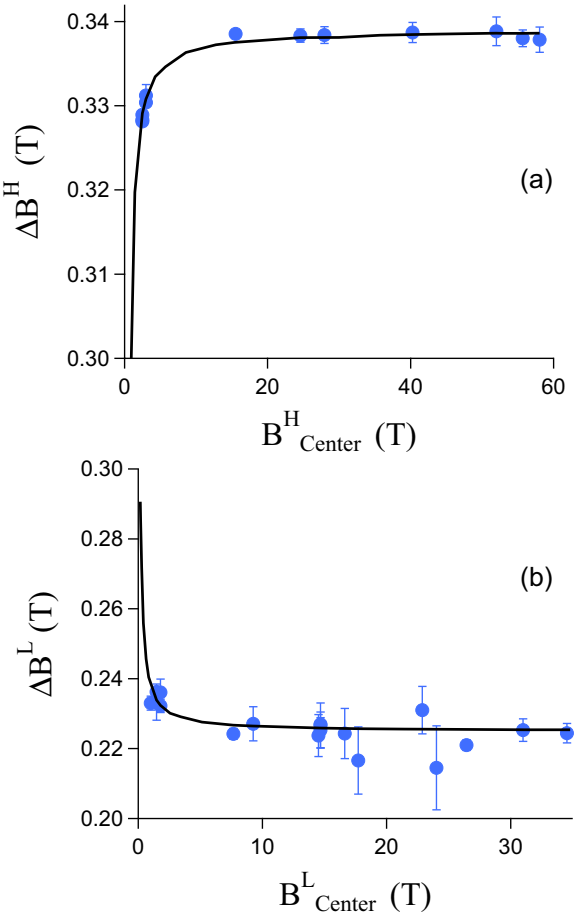

FIG. 6. Hyperfine interaction splitting of the σ^+Hi absorption lines, in (a), and σ^+Li, in (b), versus the magnetic field center of those lines. Dots for the experimental data with their error bars, and theoretical predictions derived from the Hamiltonan eigenenergies. The constant values at high field correspond to the predictions of the hyperfine or fine Paschen-Back regime. The $g_{5P_{3/2}}$ value of Eq. (10) is inserted into the theoretical analysis.

low magnetic fields, agrees qualitatively with the measured increase at high magnetic fields.

By exploring the role of the g-factor values on the high field slope of the $B^H_{\text{Center}}/B^L_{\text{Center}}$ ratio, we find that the experimental data can be reproduced by modifying g_L and g_S. Several contributions modify those values, as perturbations by excited core states [37], configuration mixing [38], combined action of exchange core polarization and spin-orbit interaction [35], and relativistic and QED corrections [32–35]. By scanning the [g_L,g_S] plane we reach a good agreement between theory and experiment as shown by the red continuous line in Fig. 5. The data are fitted by all the values lying on the line segment bounded by the [$g_L = 1.0012(2)$, $g_s = g_{5S}$] and [$g_L = 1.0$, $g_s = 2.0049(2)$] points. The first extreme assumes that an atomic perturbation modifies the g_L-factor of the $5P$ state without modification of g_S. The second extreme assumes no perturbation on g_L and a g_S increase larger than the predicted relativistic and QED corrections. Because our single result cannot discriminate between all these mechanisms, only an atomic physics theoretical calculation may determine the precise corrections for the g-factors. The [g_L,g_S] combinations lying on the above segment lead to very close values for the $5P_{3/2}$ Landé factor globally described by

$$g_{5P_{3/2}} = 1.33494(15), \tag{10}$$

with included error propagation. This value lies between the one reported in the review [16] and that derived in Sec. II D from our reanalysis of the level crossing of Ref. [30]. It is more precise than both of them.

Owing to the 5×10^{-4} fractional difference between the above $g_{5P_{3/2}}$ value and the Russel-Saunders starting value, the linear relation between B_{PU} and B_{H4} of Sec. III is modified by a quantity roughly equal to the error bar of that relation.

C. Hyperfine structure

As a test of the comparison between experimental results and theoretical predictions, we have examined the magnetic field separations between the nuclear components of the σ^+Hi and σ^+Li lines. We have measured the ^{87}Rb quantities $\Delta B^{\text{H}} = B_{\text{H4}} - B_{\text{H1}}$ and $\Delta B^{\text{L}} = B_{\text{L1}} - B_{\text{L4}}$ as a function of BH_{Center} and BL_{Center}, respectively. The data and the theoretical predictions are plotted in Fig. 6. For the few experimental data having large error bars, the input fiber Faraday rotation reduces the fluorescence signal intensity and deteriorates the spectra fitting procedure. The nuclear structure is entirely produced by

the hyperfine coupling between electronic and nuclear spins, because owing to the $\Delta m_I = 0$ selection the nuclear Zeeman energy does not modify the resonant frequency. Within the hyperfine Paschen-Back regime where **J** and **I** are fully decoupled, the m_I levels are nearly equally spaced, producing a constant frequency separation, as shown in Figs. 1(b) and 1(d). That is not true at the low B fields where **F** is the good quantum number. This difference explains why the theoretical curves rise or fall before saturating to a well-defined value. The experimental and/or theoretical agreement demonstrates the precision of our measurements and the correctness of the atomic eigenenergy derivation.

The hyperfine Paschen-Back regime is reached for $\mu_B B$ larger than the ground state hyperfine splitting. For rubidium Sec. II A places this transition around 0.5 T. Instead the data of Fig. 6 demonstrate that the transition takes place at different magnetic fields, starting roughly around 0.4 or 1.5 T depending on the observable, and terminating at higher fields. The excited state Landé g-factor determines the magnetic field amplitudes where constant values of ΔB^{H} and ΔB^{L} are reached. However, the smooth transitions between the different regimes and our error bars do not allow a determination of the g-factor. Notice that while the g-factor of Eq. (10) was used for the theoretical predictions of the figure, the use of the Russell-Saunders produces theoretical curves modified on their high-field value, but with no visible modification in the transition regions.

V. CONCLUSION

We have performed high resolution spectroscopy of a rubidium optical transition at a field slightly larger than 58 T. Our Rb sensor shows performances more than an order of magnitudes better than standard pick-up coils in terms of uncertainty, compactness and direct access to a micrometer-size explored region.

The high precision data collected in a 2 wk run at the LNCMI facility allowed an investigation of the atomic response for high magnetic fields not fully explored previously. We have investigated in detail the transition between different magnetic regimes. We were forced to analyze theoretically our data on the basis of a treatment typically applied only to the fine Paschen-Back regime, even operating at magnetic fields lower than those naively associated to that regime. The focus of our experiment was to test rubidium atom as a magnetometer; therefore we have not accumulated enough data, as for the Pi lines, and none for the σ^- transitions. A complete investigation will increase the precision of the measured excited state Landé g-factor.

While our work relies on the Doppler limited absorption spectroscopy, the application of sub-Doppler spectroscopy will lead to an increased resolution by a factor hundred. In our setup the observation of sub-Doppler absorption features relies on technical improvements. Another straightforward way to improve the probe precision is to operate with a cell containing a single rubidium isotope.

Our rubidium magnetometry accuracy is presently limited by the $g_{5P3/2}$ value, whose precision even if improved by us cannot yet compete with the hydrogen nuclear magnetic resonance. When the precision of the g-factor and of the diamagnetic corrections will be improved, the Rb magnetometer accuracy could compete with the hydrogen NMR magnetometer.

Our results opens the way to dilute matter optical tests in high magnetic fields. Precise measurements of g-factors of excited states at a level interesting to verify QED predictions appear feasible. The use of other atomic transitions or of very narrow optical transitions as in alkaline earths will expand the atomic physics at high magnetic fields and its applications.

ACKNOWLEDGMENTS

This research has been partially supported through NEXT (Grant No. ANR-10-LABX-0037) in the framework of the "Programme des Investissements d'Avenir." E.A. acknowledges financial support from the Chair d'Excellence Pierre de Fermat of the Conseil Regional Midi-Pyrenées. The authors thank S. George, N. Bruyant, J. Béard, and S. Scotto for technical support and are grateful to R. Mathevel for very useful suggestions on the manuscript.

[1] I. K. Kominis, T. W. Kornack, J. C. Allred, and M. V. Romalis, Nature (London) **422**, 596 (2003).

[2] M. Vengalattore, J. M. Higbie, S. R. Leslie, J. Guzman, L. E. Sadler, and D. M. Stamper-Kurn, Phys. Rev. Lett. **98**, 200801 (2007).

[3] H. J. Mamin, M. Poggio, C. L. Degen, and D. Rugar, Nat. Nano **2**, 301 (2007).

[4] J. M. Taylor, P. Cappellaro, L. Childress, L. Jiang, D. Budker, P. R. Hemmer, A. Yacoby, R. Walsworth, and M. D. Lukin, Nat. Phys. **4**, 810 (2008).

[5] L. M. Pham, D. L. Sage, P. L. Stanwix, T. K. Yeung, D. Glenn, A. Trifonov, P. Cappellaro, P. R. Hemmer, M. D. Lukin, H. Park, A. Yacoby, and R. L. Walsworth, New J. Phys. **13**, 045021 (2011).

[6] L. Rondin, J.-P. Tetienne, T. Hingant, J.-F. Roch, P. Maletinsky, and V. Jacques, Rep. Progr. Phys. **77**, 056503 (2014).

[7] F. Budker, D. Derek, and J. Kimball, *Optical Magnetometry* (Cambridge University Press, Cambridge, 2013).

[8] W. B. Garn, R. S. Caird, D. B. Thomson, and C. M. Fowler, Rev. Sci. Instrum. **37**, 762 (1966).

[9] H. Hori, M. Miki, and M. Date, J. Phys. Soc. Japan **51**, 1566 (1982).

[10] M. R. Gomez, S. B. Hansen, K. J. Peterson, D. E. Bliss, A. L. Carlson, D. C. Lamppa, D. G. Schroen, and G. A. Rochau, Rev. Sci. Instrum. **85**, 11E609 (2014).

[11] J. T. Banasek, J. T. Engelbrecht, S. A. Pikuz, T. A. Shelkovenko, and D. A. Hammer, Rev. Sci. Instrum. **87**, 103506 (2016).

[12] S. George, N. Bruyant, J. B. Béard, S. Scotto, E. Arimondo, R. Battesti, D. Ciampini, and C. Rizzo, Rev. Sci. Instrum. **88**, 073102 (2017).

[13] H. Kopfermann, *Nuclear Moments* (Academic Press, New York, 1958).

[14] S. J. Lipson, G. D. Fletcher, and D. J. Larson, Phys. Rev. Lett. **57**, 567 (1986).
[15] N. Fortson, Phys. Rev. Lett. **59**, 988 (1987).
[16] E. Arimondo, M. Inguscio, and P. Violino, Rev. Mod. Phys. **49**, 31 (1977).
[17] C. Foot, *Atomic Physics* (Oxford University Press, Oxford, 2012).
[18] L. Schiff and H. Snyder, Phys. Rev. **55**, 59 (1939).
[19] R. Garstang, Rep. Progr. Phys. **40**, 105 (1977).
[20] P. Otto, M. Gamperling, M. Hofacker, T. Meyer, V. Pagliari, A. Stifter, M. Krauss, and W. Hüttner, Chem. Phys. **282**, 289 (2002).
[21] F. Jenkins and E. Segrè, Phys. Rev. **55**, 52 (1939).
[22] D. Harting and P. Klinkenberg, Physica **14**, 669 (1949).
[23] C. Harper and M. Levenson, Opt. Commun. **20**, 107 (1977).
[24] W. Hüttner, P. Otto, and M. Gamperling, Phys. Rev. A **54**, 1318 (1996).
[25] T. Gallagher, *Rydberg Atoms* (Cambridge University Press, Cambridge, 1994).
[26] W. Li, I. Mourachko, M. W. Noel, and T. F. Gallagher, Phys. Rev. A **67**, 052502 (2003).
[27] D. Steck, Rubidium 87 D line data, 2001, george.ph.utexas.edu/dsteck/alkalidata rubidium87numbers.pdf (2001).
[28] J. S. Tiedeman and H. G. Robinson, Phys. Rev. Lett. **39**, 602 (1977).
[29] P. J. Mohr, D. B. Newell, and B. N. Taylor, Rev. Mod. Phys. **88**, 035009 (2016).
[30] G. Belin and S. Svanberg, Phys. Scr. **4**, 269 (1971).
[31] J. Ye, S. Swartz, P. Jungner, and J. L. Hall, Opt. Lett. **21**, 1280 (1996).
[32] L. Labzowsky, I. Goidenko, and P. Pyykkö, Phys. Lett. A **258**, 31 (1999).
[33] I. Goidenko, L. Labzowsky, G. Plunien, and G. Soff, Phys. Rev. A **66**, 032115 (2002).
[34] P. Indelicato, J. P. Santos, S. Boucard, and J.-P. Desclaux, Eur. Phys. J. D **45**, 155 (2007).
[35] G. H. Gossel, V. A. Dzuba, and V. V. Flambaum, Phys. Rev. A **88**, 034501 (2013).
[36] F. Debray and P. Frings, C. R. Phys. **14**, 2 (2013).
[37] M. Phillips, Phys. Rev. **88**, 202 (1952).
[38] W. J. Childs and L. S. Goodman, Phys. Rev. A **3**, 25 (1971).